

Inversion of magnetic data for magnetization and source depth

Title:		
Inversion of magnetic data for magnetization and source depth		
Document no.:	Contract no.:	Project: Seabed Exploration and DEEPEN

Classification: Open	Distribution:
Expiry date:	Status: Draft

Distribution date: 07.12.2021	Rev. no.:	Copy no.:
---	-----------	-----------

Author(s)/Source(s): Ketil Hokstad (RLC EPS EPC)	
Subjects: Magnetic inversion Deep-sea mineral exploration Hydrothermal exploration	
Remarks:	
Valid from: 2021-12-07	Updated:
Responsible publisher:	Authority to approve deviations:

Prepared by (Organisation unit / Name): Ketil Hokstad (RLC EPS EPC)	Date/Signature: <u> X </u>
Responsible (Organisation unit/ Name):	Date/Signature: <u> X </u>
Recommended (Organisation unit/ Name):	Date/Signature: <u> X </u>
Approved by (Organisation unit/ Name):	Date/Signature: <u> X </u>

Summary

Young mid-oceanic ridge basalts possess high level of magnetization, dominated by natural remanent magnetization. This is evident from the characteristic striping of the seabed on oceanic crust, which record the flips of the earth magnetic field through the history of the earth. Zones of elevated temperature will have reduced magnetization. At the Curie temperature, the fingerprint of magnetic minerals, the magnetic properties of the rock will change from ferromagnetic to paramagnetic. Equally important is destruction of magnetization due to interaction of basaltic rocks and hydrothermal fluids flowing through the pores and fractures of the rock. The destruction the magnetic minerals and magnetization is permanent and remains also after the extinction of the hydrothermal system. Consequently, the analysis of magnetic properties of basalts is of interest for both geothermal exploration and seabed massive sulfide exploration. In both cases, hydrothermal circulation plays an important role.

The first stage of a quantitative analysis of magnetic properties of mid-oceanic ridge basalt is the inversion of potential-field magnetic data to estimate the magnetization of the rocks. The magnetization is magnetic dipole moment per unit volume. This includes both the remanent part, which remains also in the absence of an external field, and the induced part, which is the response of the magnetic rock to the presence of the earth's magnetic background field.

Here we present an inversion scheme which for inversion of magnetic data, to obtain estimates the magnetization, and optionally also estimates of the depth to the base of a magnetic source layer. Inversion for magnetization, with a fixed source depth is a linear inverse problem, which can be solved in one step. Inversion for the base of the magnetic source layer is a non-linear inverse problem, which can be solved iteratively by the Gauss-Newton scheme. Two different inversion strategies can be used: (1) Linear inversion for magnetization with fixed base of source layer, followed by iterative updates of the base with fixed magnetization. (2) Simultaneous iterative updates of both magnetization and depth of source layer. The first alternative is more robust. In both cases, the first iteration is a linear inversion step.

It is well-known that inversion of potential field data (gravity and magnetics) constitutes an ill-posed inverse problem. The information available in potential field data is quite limited, since different from e.g. seismic data, there is no temporal bandwidth. However, Potential field data provides a range of spatial wavenumbers (or wavelengths). The magnetic flux decays as inverse distance cube away from magnetic sources. Therefore, small wavenumbers (large wavelengths) are sensitive to deep structure, whereas high wavenumbers (short wavelengths) are sensitive only to shallow features. To utilize these properties, an inversion strategy based on decomposition of magnetic data in radial wavenumber bands was developed. In this way, some information about the depth of the magnetic sources can be obtained.

Matrix inversions are performed using the Moore-Penrose pseudo inverse, and the Marquardt-Levenberg algorithm. Computer codes were implemented in **Python**, using linear algebra and Fourier transform in the **numpy** and **scipy** modules.

The proposed inversion scheme and inversion strategy is first demonstrated and tested on synthetic data from simple models. Then the inversion methodology is applied to magnetic data from an (onshore) geothermal area on Iceland, and to the (offshore) Mohn's Ridge north of the Jan Mayen island.

The proposed magnetic inversion scheme can easily be adapted for gravity inversion, by replacing the magnetic forward modeling function by the corresponding gravity forward model.

Table of contents

1	Introduction	5
2	Magnetic forward model.....	6
3	Inversion scheme.....	8
4	Inversion of wavenumber ranges.....	10
5	Synthetic data examples	11
6	Geothermal example.....	18
7	Seabed massive sulfide example	20
8	Conclusions	27
9	Acknowledgements	27
10	References.....	28
11	Appendix: Gravity forward model	30

1 Introduction

The magnetic properties of mid-oceanic ridge basalts have been studied extensively since the classical work of Vine et al (1963). They proposed that the alternating pattern of seabed lineaments with positive and negative magnetization was associated with sea floor spreading and reversals of the earth magnetic field. This complicates the analysis of rock magnetism for rocks that have experienced several flips of the magnetic field and tectonic movement away from the position of crystallization of the rock.

Detailed analysis of the magnetic properties of old rocks requires estimates of both the paleomagnetic field and plate tectonic reconstructions to estimate the geographical origin of the rocks. Young mid-oceanic ridge basalts (MORB) are of special interest, since these complications are less pronounced. Iceland constitutes a special case, where the Mid-Atlantic Ridge can be studied onshore. Also, such investigations are of practical and commercial interest for geothermal exploration (Dietze et al., 2010; Olivia-Urcia et al., 2011; Hokstad et al., 2020), and more recently, deep-sea mineral exploration (Sztikar et al., 2014).

The magnetization of minerals and rocks may be viewed as a battle between quantum-mechanical order and thermal disorder (Ising, 1925). The transition between the two domains take place around the Curie/Neel temperature. Below the Curie temperature the rock is ferromagnetic or ferrimagnetic. Above the Curie temperature, only a weak paramagnetism or diamagnetism remains. For this reason, we expect that magnetic data and magnetization may be a useful source of information about the presence of both working and extinct hydrothermal systems.

The initial magnetic mineralogy of mid-oceanic ridge basalts varies within a relatively narrow range with 60 % ulvöspinel and 40% magnetite, and is often referred to as TM60 (Johnson and Hall, 1977, McElhinny and McFadden, 2000; Koichira and Kikawa, 1988). After the deposition, the basalts go through oxidation and possibly hydrothermal alteration, following low-temperature or high-temperature cooling paths, as discussed by Pariso and Johnson (1991). The alteration history of the basalts may be complex, but common to these processes are that they tend to reduce the magnetization compared to the initial TM60 composition.

Titanomagnetite is known to be a solid solution of ulvöspinel and magnetite, formed when the basaltic lavas are cooled and solidified. Upon further cooling, the solid solution becomes unstable. Exsolution occurs when the titanomagnetite enters the miscibility gap of the phase diagram and leads to the decomposition of an initially homogeneous titanomagnetite into ulvöspinel-rich and magnetite-rich phases (Yund, and McAllister, 1969; Hokstad et al., 2020). Inversion of potential-field data is ill-posed. Without strong regularization or simplifications of the inverse problem, a meaningful solution to the inverse problem cannot be obtained (Li and Oldenburg, 1996). For this reason, the analysis of magnetic data has traditionally been dominated by forward modeling studies, or a combination of modeling and inversion (Quesnel et al., 2008).

The magnetic field decays as inverse distance cube away from the magnetic sources, and with a dipole pattern. The magnetic forward modeling operator, i.e. the solution to the magnetostatic equation, can consequently be viewed as a defocusing operator. The inverse (in practice, the pseudo inverse) operator can correspondingly be viewed as a focusing operator, in analogy with seismic imaging. Magnetic inversion is therefore of interest to obtain higher resolution images of the magnetization. This is of particular interest when the magnetic targets have small size, for instance for mapping seabed massive sulfide (SMS) deposits.

In this work, we derive and present an inversion scheme for estimation of both the magnitude of the magnetization, and the depth of the magnetic source layer. The first step is a linear inversion to estimate the magnetization, given an initial depth of the magnetic source layer. Then follows an iterative Gauss-Newton iteration, to update the magnetization and the source depth. We then apply this fundamental inversion algorithm to different wavenumber ranges, to obtain a magnetization model which to some degree can resolve the depth of various magnetic anomalies.

The proposed inversion methodology is demonstrated for both onshore and offshore applications, for geothermal and deep-sea mineral exploration, respectively. The geothermal example is from the Hellisheidi geothermal area on Iceland. In the deep sea-mineral example from the Mohn's Ridge, north of the Jan Mayen island, the inversion scheme is applied to both aeromagnetic data from Equinor's database, and high-resolution data measured from an autonomous under-water vehicle (AUV).

Regarding fonts in equations: We write vectors in 3-dimensional physical space in ***italic bold font***. We write vectors and matrices in n -dimensional Hilbert space in **non-italic bold font**.

2 Magnetic forward model

Magnetic anomaly data are due to dipole sources in the subsurface. The anomalous magnetic field vector \mathbf{B}_A can be expressed as a double differentiation of an inverse-distance potential (Blakely, 1996)

$$\mathbf{B}_A(\mathbf{x}) = -\frac{\mu_0}{4\pi} \nabla \nabla \cdot \iiint \frac{\mathbf{M}(\mathbf{x}')}{|\mathbf{x}' - \mathbf{x}|} dV', \quad (1)$$

where \mathbf{M} is the magnetization vector, $\mathbf{x}' = (x', y', z')$ denotes the positions of magnetic sources, $\mathbf{x} = (x, y, z)$ is the position where the magnetic field is observed, μ_0 is the vacuum permeability, and $dV' = dx' dy' dz'$ is the volume differential. In standard acquisition of magnetic potential-field data, only the magnitude of the total magnetic field, the total magnetic intensity, is measured,

$$B_{TMI} = |\mathbf{B}_0 + \mathbf{B}_A| = \sqrt{|\mathbf{B}_0|^2 + |\mathbf{B}_A|^2 + 2\mathbf{B}_0 \cdot \mathbf{B}_A}, \quad (2)$$

where \mathbf{B}_0 is the earth magnetic background field. The scalar total magnetic anomaly B_A is obtained by subtracting the magnitude of the local magnetic field,

$$B_A = |\mathbf{B}_0 + \mathbf{B}_A| - |\mathbf{B}_0|. \quad (3)$$

Expanding the square-root to 2nd order in \mathbf{B}_A , the scalar total magnetic anomaly can be written as

$$B_A \simeq \mathbf{t} \cdot \mathbf{B} + \frac{|\mathbf{t} \times \mathbf{B}_A|^2}{|\mathbf{B}_0|}, \quad (4)$$

where $\mathbf{t} = \mathbf{B}_0/|\mathbf{B}_0|$ is a unit vector in the direction of \mathbf{B}_0 . When $|\mathbf{B}_A| \ll |\mathbf{B}_0|$, the second term is insignificant, and the scalar magnetic field B_A is approximately the projection of the anomalous field onto the direction of the earth magnetic background field. This assumption is used in the following.

Magnetic data capture lateral changes in magnetization, but with limited depth resolution. Therefore, 3D magnetic inversion is ill-posed, and must be constrained to give meaningful results (e.g. Li and Oldenburg, 1996; Hokstad et al., 2017). The depth distribution of magnetic anomalies from 3D inversion is to a large degree controlled by the regularization used and should not be over-interpreted. In the present work, we use a map-inversion method to circumvent this problem. Correspondingly, for the forward model, we assume that the magnetization is independent of depth, or it represents an average over the depth range z_1 to z_2 , such that

$$\mathbf{M}(x, y) = \frac{1}{z_2 - z_1} \int_{z_1}^{z_2} \mathbf{M}(x, y, z) dz. \quad (5)$$

Then the integral over z' in equation (1) can be carried out to obtain,

$$\int_{z_1}^{z_2} \frac{1}{r} dz' = \ln[(z' - z) + r] \Big|_{z_1}^{z_2} = F(z_2) - F(z_1). \quad (6)$$

For later convenience, we have introduced the radial distance $r = \sqrt{(x' - x)^2 + (y' - y)^2 + (z' - z)^2}$, and the function

$$F(z') = \ln[(z' - z) + r], \quad (7)$$

where the notation $F(z')$ emphasize the dependence magnetic source depth. Substituting equation (6) in equation (1) and using equation (4), the scalar magnetic anomaly B_A can be written approximately as

$$B_A(x) \simeq \mathbf{t} \cdot \mathbf{B}_A(x) = \frac{\mu_0}{4\pi} \sum_{i=1}^3 \sum_{j=1}^3 \iint t_i A_{ij}(x, x') M_j(x', y') dx' dy', \quad (8)$$

where t_i and M_j are elements of the vectors \mathbf{t} and \mathbf{M} , respectively, the sums run over $(x_1, x_2, x_3) = (x, y, z)$, and A_{ij} are the elements of a second-order tensor given by

$$A_{ij} = \frac{\partial^2 F(z_2)}{\partial x_i \partial x_j} - \frac{\partial^2 F(z_1)}{\partial x_i \partial x_j} \quad (9)$$

where

$$\begin{aligned} \frac{\partial^2 F(z')}{\partial x_i \partial x_j} = & -\frac{1}{[(z' - z) + r]^2} \left[\delta_{i3} + \frac{(x'_i - x_i)}{r} \right] \left[\delta_{j3} + \frac{(x'_j - x_j)}{r} \right] \\ & + \frac{1}{[(z' - z) + r]} \left[\frac{\delta_{ij}}{r} - \frac{(x'_i - x_i)(x'_j - x_j)}{r^3} \right] \end{aligned} \quad (10)$$

The derivatives are with respect to the coordinates $(x_1, x_2, x_3) = (x, y, z)$ of the observation point, and δ_{ij} is the Kronecker delta.

Equations (8) to (10) are equivalent to the results presented by Bhattacharyya (1964) (his equation 7). From equation (8), it's clear that the three-component magnetization vector \mathbf{M} cannot be readily obtained by inversion of scalar data B_A . However, if the direction of magnetization is approximately known, we can attempt to invert for the

magnitude, which is a more feasible problem. Hence, we write $\mathbf{M} = M\mathbf{e}$ where M and \mathbf{e} are the magnitude and direction of the magnetization, respectively. For young igneous rocks, such as MORB, it is reasonable to assume $\mathbf{e} = \mathbf{t}$.

For later use in inversion, we discretize the integral over magnetic source locations. Then the forward model for the magnetic anomaly observed at location \mathbf{x}_i due to magnetic sources at \mathbf{x}'_j can be written as

$$B_A(\mathbf{x}_i) = \sum_j Q_M(\mathbf{x}_i, \mathbf{x}'_j) M(\mathbf{x}'_j), \quad (11)$$

where

$$Q_M(\mathbf{x}_i, \mathbf{x}'_j) = \frac{\mu_0}{4\pi} \Delta S'_j \sum_{k=1}^3 \sum_{l=1}^3 t_k A_{kl}(\mathbf{x}_i, \mathbf{x}'_j) e_l, \quad (12)$$

and $\Delta S'_j = \Delta x'_j \Delta y'_j$ is the surface element associated with source location \mathbf{x}'_j . Using equation (6), it's obvious that the derivative of Q_M with respect to z_2 is given by the familiar 3D magnetic-field solution (Blakely, 1996)

$$\frac{\partial Q_M}{\partial z_2} = \frac{\mu_0}{4\pi} \Delta S'_j \sum_{k=1}^3 \sum_{l=1}^3 t_k \left[\frac{\partial}{\partial z_2} \frac{\partial^2 F(z_2)}{\partial x_k \partial x_l} \right] e_l, \quad (13)$$

$$\frac{\partial}{\partial z_2} \frac{\partial^2 F(z_2)}{\partial x_i \partial x_j} = -\frac{\delta_{ij}}{r_{ij}^3} + 3 \frac{(x'_i - x_i)(x'_j - x_j)}{r_{ij}^5}. \quad (14)$$

3 Inversion scheme

As the starting point for development of a non-linear inversion scheme (Tarantola, 1984), we assume that the observed data can be represented as

$$\mathbf{d} = \mathbf{f}(\mathbf{m}) + \mathbf{n}. \quad (15)$$

Then the L_2 objective function Φ can be written as

$$\Phi = \frac{1}{2} [\mathbf{d} - \mathbf{f}(\mathbf{m})]^T [\mathbf{d} - \mathbf{f}(\mathbf{m})] + \lambda \frac{1}{2} \mathbf{m}^T \mathbf{D}^T \mathbf{D} \mathbf{m}, \quad (16)$$

We use the common vector and matrix notation for data and model parameters, where \mathbf{d} is data, \mathbf{m} is model parameters, $\mathbf{f}(\mathbf{m})$ is the discretized forward model, given in equations (11) and (12), acting on \mathbf{m} , and \mathbf{n} is noise. The first term in the objective function represents the contribution from data misfit, and the second term accounts for prior information and regularization. The regularization matrix \mathbf{D} will be considered later. Assuming Gaussian distributions with diagonal covariance matrices for the data noise and prior/regularization, $\lambda = \sigma_m / \sigma_n$ controls the relative contributions of data misfit and regularization in the objective function. The model-vector \mathbf{m} consists of two types of model parameters

$$\mathbf{m} = [\mathbf{M}, \mathbf{z}_2]^T \quad (17)$$

where $\mathbf{M} = [M(x'_1), M(x'_2), \dots, M(x'_n)]^T$ is the scalar magnetization of the subsurface, and $\mathbf{z}_2 = [z_2(x'_1), z_2(x'_2), \dots, z_2(x'_n)]^T$ is the base of the magnetic-source layer. The gradient of the objective function with respect to model parameters is given by

$$\mathbf{g} = \frac{\partial \Phi}{\partial \mathbf{m}}. \quad (18)$$

For a given model vector \mathbf{m} , we seek a model update $\Delta \mathbf{m}$ such that the objective function reaches a minimum given by

$$\mathbf{g}(\mathbf{m} + \Delta \mathbf{m}) = \mathbf{g}(\mathbf{m}) + \frac{\partial \mathbf{g}}{\partial \mathbf{m}} \Delta \mathbf{m} = 0$$

The model update $\Delta \mathbf{m}$ can then be computed by

$$\Delta \mathbf{m} = -\mathbf{H}^{-1}(\mathbf{m})\mathbf{g}(\mathbf{m}), \quad (19)$$

Which will subsequently be used in an iterative loop. The Hessian matrix is given by

$$\mathbf{H} = \frac{\partial \mathbf{g}}{\partial \mathbf{m}} = \frac{\partial^2 \Phi}{\partial \mathbf{m}^2}. \quad (20)$$

By differentiation of equation (16), the gradient and Hessian are obtained as

$$\mathbf{g} = \mathbf{J}^T[\mathbf{d} - \mathbf{f}(\mathbf{m})] + \lambda \mathbf{D}^T \mathbf{D} \mathbf{m}, \quad (21)$$

and

$$\mathbf{H} \simeq \mathbf{J}^T \mathbf{J} + \lambda \mathbf{D}^T \mathbf{D}, \quad (22)$$

where we have omitted the 2nd derivative of the forward model $\mathbf{f}(\mathbf{m})$. The Jacobian matrix \mathbf{J} is the derivative of the forward model with respect to model parameters, and consists of two parts

$$\mathbf{J} = \frac{\partial \mathbf{f}}{\partial \mathbf{m}} = [\mathbf{L}, \mathbf{K}]. \quad (23)$$

The elements of the submatrices \mathbf{L} and \mathbf{K} are obtained from equations (11) to (13) as

$$L_{ij} = Q(x_i, x'_j), \quad (24)$$

and

$$K_{ij} = \frac{\partial Q(x_i, x'_j)}{\partial z_2(x'_j)} M(x'_j). \quad (25)$$

The regularization matrix $\mathbf{D}^T \mathbf{D}$ can be chosen in different ways. In our implementation we have used the Marquardt-Levenberg scheme, with the regularization

$$\mathbf{D}^T \mathbf{D} = \text{diag}(\mathbf{J}^T \mathbf{J}). \quad (26)$$

Using the equations above, the model parameters \mathbf{m} are updated in a nonlinear iterative inversion by

$$\mathbf{m}_{k+1} = \mathbf{m}_k + \Delta \mathbf{m}_k, \quad (27)$$

where the subscript k is the iteration number. The magnetic forward model in equation (11) is linear in the magnetization $M(x, y)$ and nonlinear in the base of the source layer $z_2(x, y)$. If the initial value for the magnetization is taken to be zero, $\mathbf{M}_0 = 0$, the part of the Jacobian matrix related to magnetic source depth z_2 is zero. Then, the first iteration of the inversion is linear, and equivalent to the inversion scheme presented by Hokstad et al (2020).

In the Appendix, we indicate how the magnetic inversion scheme presented above can easily be adapted for gravity data, and for the vertical gravity gradients.

4 Inversion of wavenumber ranges

Blakely (1996) and Hsieh et al (2014) define the power-density spectrum of the magnetic anomaly data by

$$P(k_r) \propto |B_A(k_x, k_y, z)|^2, \quad (28)$$

where $k_r = \sqrt{k_x^2 + k_y^2}$ is the radial horizontal wavenumber. Under the assumption of random and uncorrelated magnetization $M(x, y)$, they derive equations for the top z_1 and center z_c of the magnetic source layer,

$$\ln[|P(k_r)|^{1/2}] = \ln(a) - |k_r|z_1, \quad (29)$$

$$\ln \left[\frac{|P(k_r)|^{1/2}}{|k_r|} \right] = \ln(b) - |k_r|z_c. \quad (30)$$

The top and center of the source layer, and the intercepts $\ln(a)$ and $\ln(b)$ can be determined by linear regression. The base of the source layer can then be obtained as

$$z_2 = 2z_c - z_1, \quad (31)$$

and the thickness of the source layer is $z_2 - z_1$. Equations (28) to (31) are approximate. However, motivated by these relationships, we introduce the idea of performing inversion of separate wavenumber bands, with systematically varying depth sensitivity. More specifically, low wavenumbers are sensitive to anomalies located through the entire stack of magnetic source layers, whereas high wavenumbers are only sensitive to relatively shallow magnetic sources.

We write the magnetic anomaly data $B_A(x)$ as a sum of bandlimited datasets on ranges $[k_1^{(j)}, k_2^{(j)}]$, such that

$$\mathbf{d} = \sum_{j=1}^{N_k} \mathbf{d}^{(j)}, \quad (32)$$

and

$$B_A(x_i) = \sum_{j=1}^{N_k} B_A^{(j)}(x_i) = \sum_{j=1}^{N_k} \mathbf{f}(\mathbf{m})^{(j)}. \quad (33)$$

In practice we split the data in overlapping wavenumber bands with tapered edges such that equation (33) is fulfilled. Then we perform inversion of each wavenumber band separately, in to obtain a set of N_k submodels $\mathbf{m}^{(j)}$, with magnetization $\mathbf{M}^{(j)}$ and corresponding source depth $z_2^{(j)}$. The top of the source layer $z_1(x, y)$ is common to all submodels. The final model is then obtained as the sum over submodels

$$\mathbf{M} = \sum_{j=1}^{N_k} \mathbf{M}^{(j)}, \quad (34)$$

where N_k is the number of wavenumber ranges (typically we decompose the data into 3-5 wavenumber ranges).

5 Synthetic data examples

We start with the simplest possible synthetic model: a vertical distribution of magnetization extending over 2 grid nodes and recording of the synthetic magnetic anomaly data at an altitude of 4, 8 and 12 grid nodes above the anomaly. The physical equation (1) governing magnetostatics is scale invariant. Hence the grid spacing is not important. In the examples shown below, we assumed $\Delta x = \Delta y = \Delta z = 250\text{m}$, which implies that the depth of the source is 500m and the recording surfaces are 100m, 200m, and 300m above the top of the magnetic source, respectively. The inclination and declination are $I = 90^\circ$ and $D = 0^\circ$, which corresponds to data adjusted by reduction to pole (RTP). The regularization weight was $\lambda = 10^{-32}$.

First, we assume that both the top and base of the source are known and perform only the linear first iteration of the inversion (Figure 1). The data aperture used in the inversion was 2000m x 1600m, centered over the magnetic anomaly. The results show that, at least for a simple idealized case, the pseudo inverse of the magnetic forward operator acts as a focusing operator, as expected. If this holds also for more complex models, at least approximately, will be investigated below.

The inclination and declination can also be taken into account as part of the inversion. In order to demonstrate this, we rerun the example in Figure 1a, with $I = 45^\circ$ and $D = -25^\circ$, which corresponds to a TAG-like setting (Figure 2).

In the second numerical example, we investigate if the inversion can resolve multiple anomalies, two of them located close to each other (Figure 3). Again, the top and base of the source layer are assumed to be known, and only the linear step is performed.

In the third example, we return to the simple model with only one anomaly, to test the non-linear Gauss-Newton inversion. We estimate an initial depth of the source layer using the power-spectral method in equations (28) to (31). The thickness of the magnetic layer is estimated better than the absolute depth to the top and base (Figure 4). The initial values used for the inversion were set to $M = 0 \text{ A/m}$ for the magnetization, $z_2 = 450 \text{ m}$ for the base. The top of the anomaly was fixed at $z_1 = 0$. We simulated data at 1000m and 3000m above the anomaly, i.e. at $z = -1000\text{m}$ and $z = -3000\text{m}$. The results from the inversion show that both the magnetic anomaly appears already at the first linear iteration step, and the main effect of the non-linear inversion is to adjust the base of the anomaly downwards towards the correct depth of 500m (Figure 5 and Figure 6). The data misfit, measured in terms of RMS error, decays as expected (Figure 7).

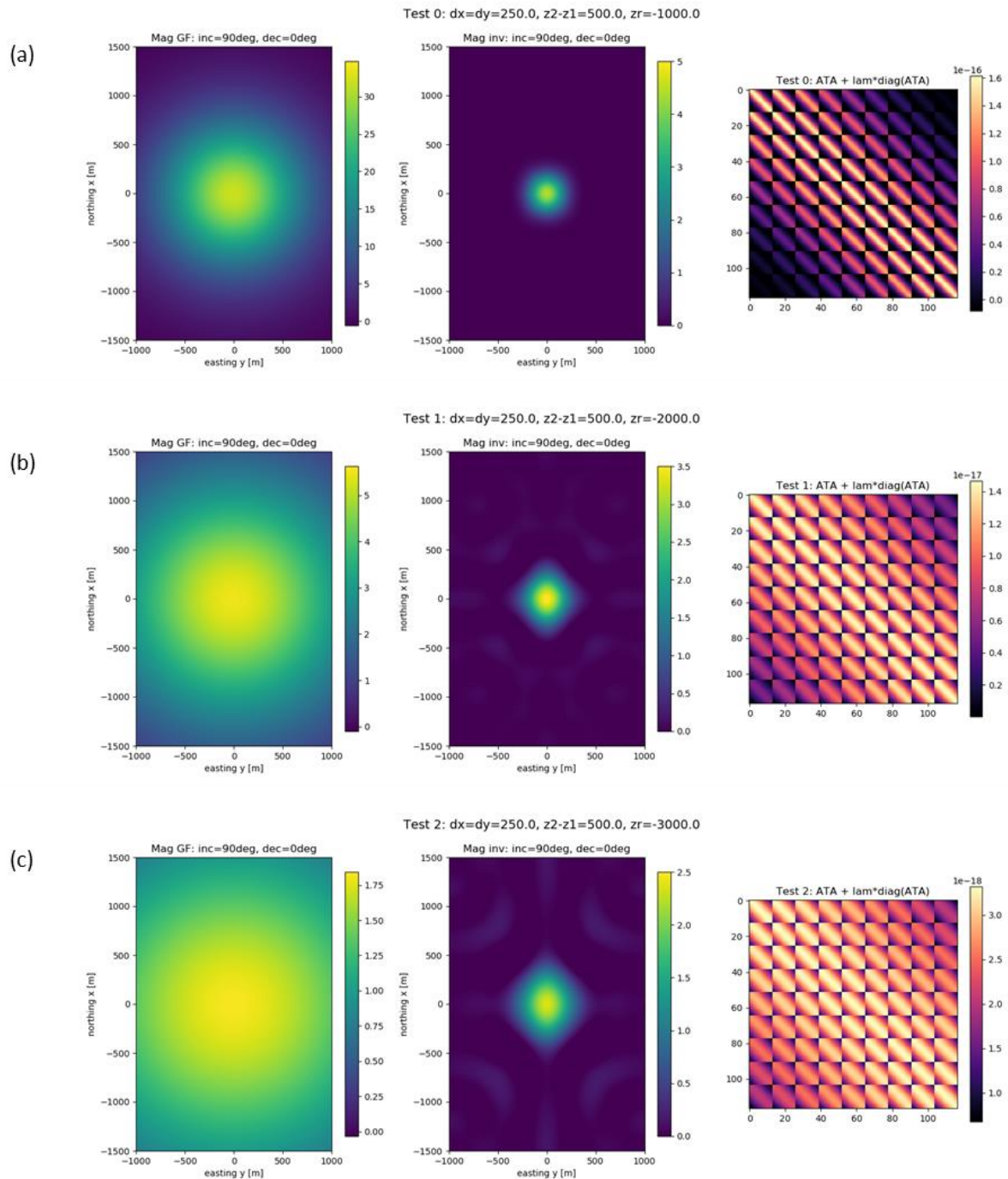


Figure 1: Inversion of magnetic anomaly data due to a single magnetic body. The synthetic data are recorded (a) 1000m above, (b) 2000m above and (c) 3000m above the source. Panels from left to right show magnetic anomaly data (in nT), magnetization (in A/m), and the structure of the Hessian matrix as given in equation (22). Only the linear inversion step is performed, with magnetic source layer thickness $z_2 - z_1 = 500\text{m}$ assumed to be known.

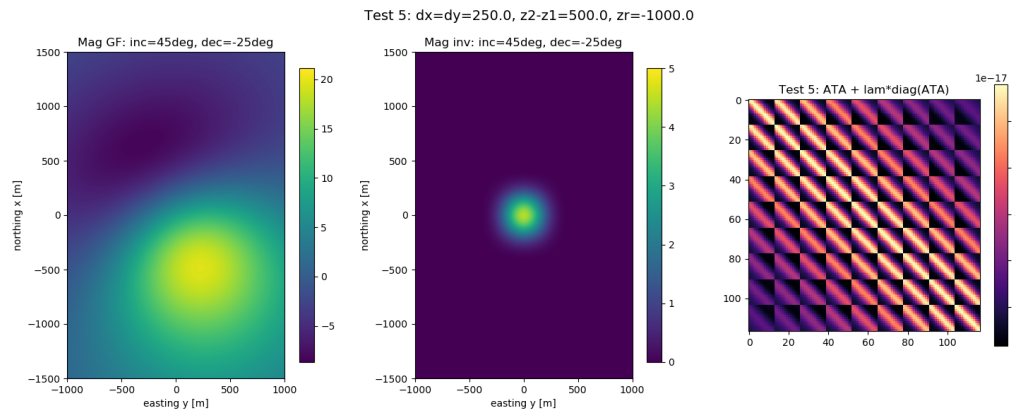


Figure 2: The example in Figure 1a, rerun with inclination $I = 45^\circ$ and declination $D = -25^\circ$. This corresponds roughly to a TAG-like geographic position.

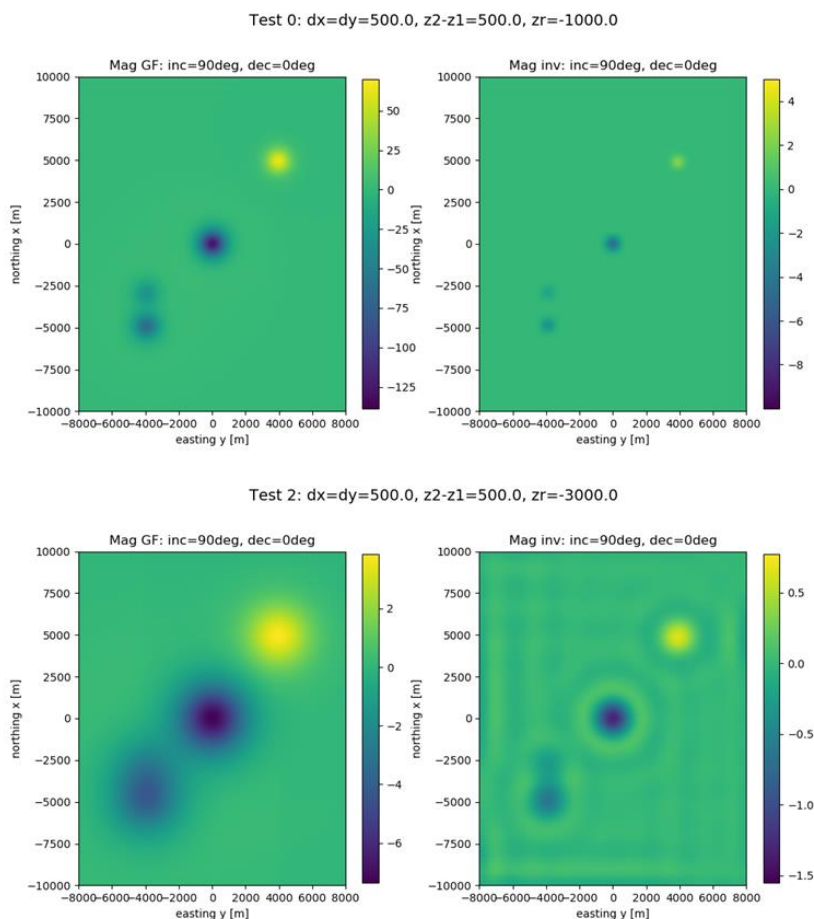


Figure 3: Inversion of data from a model with four magnetic anomalies. The synthetic data are recorded (a) 1000m above, and (b) 3000m above the source. Panels from left to right show magnetic anomaly data (in nT), magnetization from inversion (in A/m),

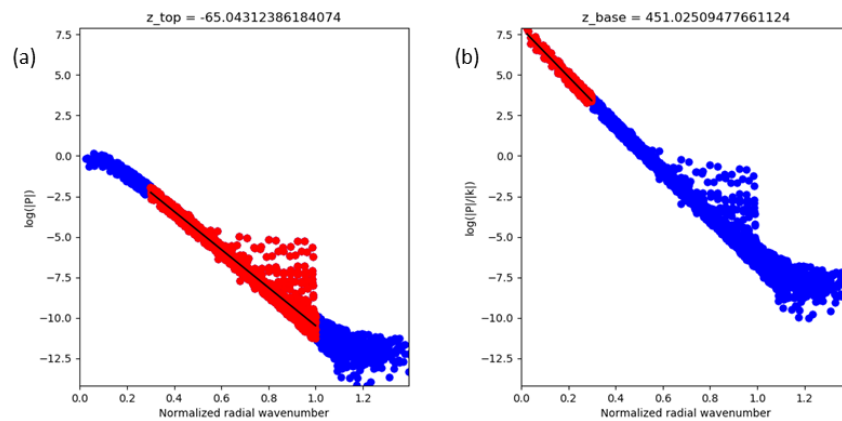


Figure 4: (a) Top and (b) base of anomaly estimated from the data by the power-spectral method in equations (28) to (31). The blue dots show the full radial power spectrum, and the red dots show the part of the spectrum used in the regression for top and base of the anomaly, respectively. The estimate of the base of anomaly, $z_2 = 450\text{m}$, was used as the initial value in the non-linear Gauss-Newton inversion. Power-spectral estimation of base of source layer have been found to perform poorly when there are multiple magnetic source layers.

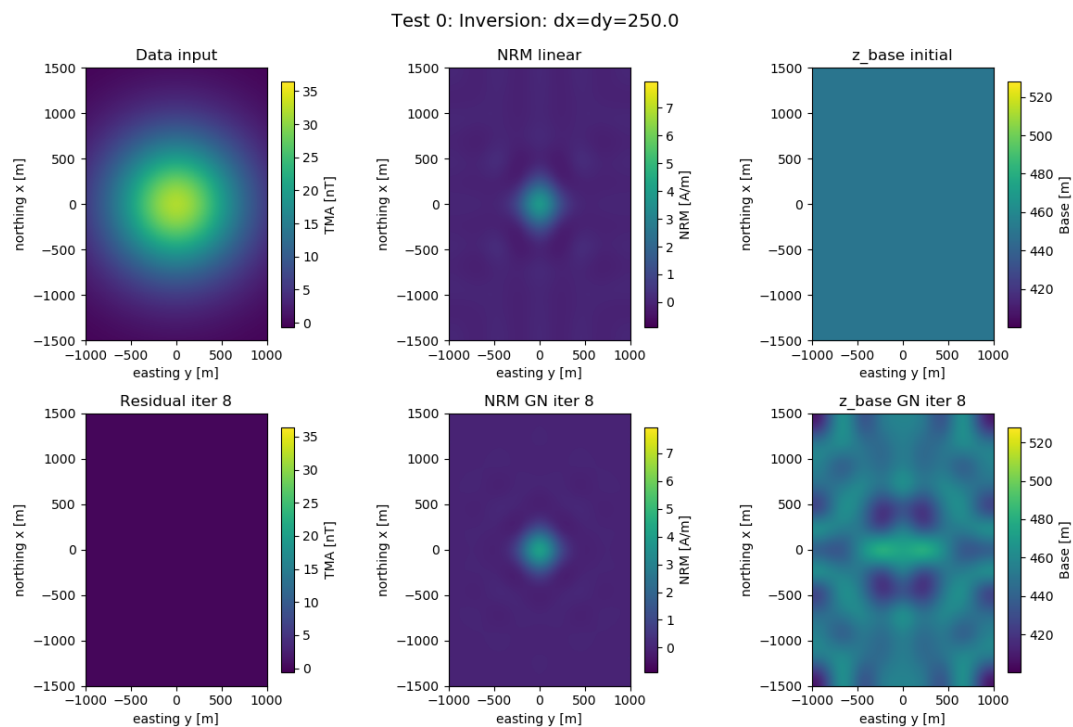


Figure 5: Non-linear Gauss-Newton inversion of synthetic data recorded 1000m above the magnetic anomaly. Top panels from left to right: input data, magnetization after first linear inversion, and base of anomaly in the linear inversion, $z_2 = 450\text{m}$. Bottom panes from left to right: Data residual, magnetization and base of anomaly after 8 Gauss-Newton iterations.

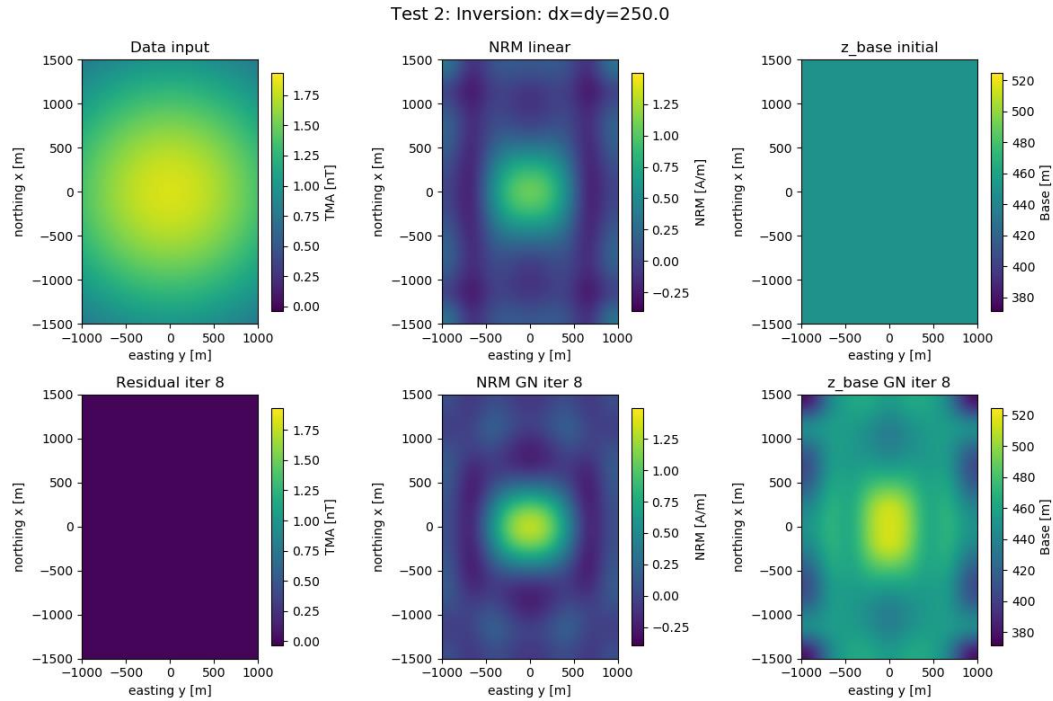


Figure 6: Non-linear Gauss-Newton inversion of synthetic data recorded 3000m above the magnetic anomaly. Top panels from left to right: input data, magnetization after first linear inversion, and base of anomaly in the linear inversion, $z_2 = 450\text{m}$. Bottom panes from left to right: Data residual, magnetization and base of anomaly after 8 Gauss-Newton iterations.

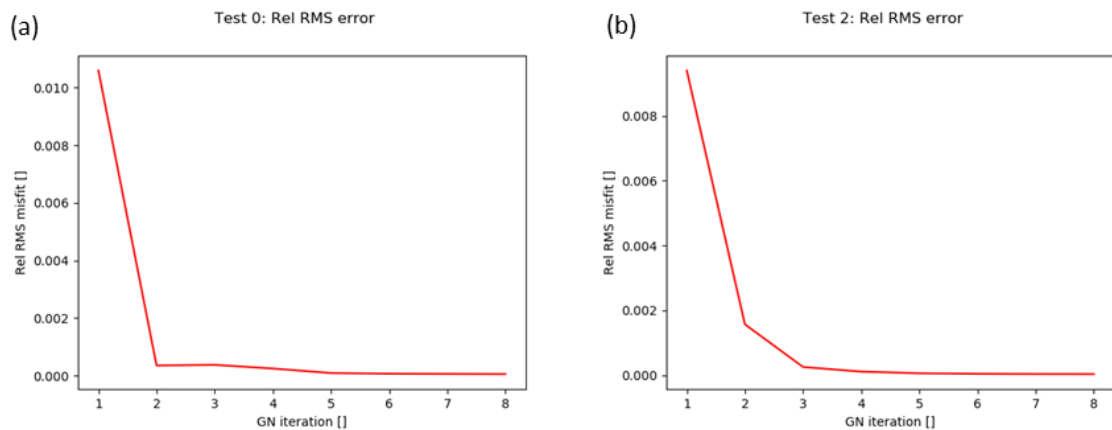


Figure 7: Data misfit for 8 iterations of non-linear Gauss-Newton inversion for the inversion examples in (a) Figure 5 and (b) Figure 6.

In the fourth, and last, synthetic example, we demonstrate the inversion of data split into wavenumber bands. The model consists of a deep ridge-like feature with top at 100m and base at 1500m. The shallow anomalies have top at 0 and base at 500m. The response of all features can be identified in the synthetic data (Figure 8). The data was decomposed into three different ranges of high, intermediate and low wavenumbers, with a tapered overlap between. The wavenumber bands were 0-15%, 15-30% and 30-60% of the Nyquist wavenumber.

The wavenumber bands were then inverted separately (Figure 9). As expected, we observe that the high wavenumbers only pick up the shallow anomalies. The intermediate wavenumbers also see the shallow anomalies, and the rim of the deeper ridge-like feature. The low wavenumbers mainly pick up the background trend, and in the present case they are dominated by the response of the deep feature, but also shows a weak imprint of the shallow anomalies. The three inversion results from each wavenumber band was added together to obtain a 3D image of the structure (Figure 10).

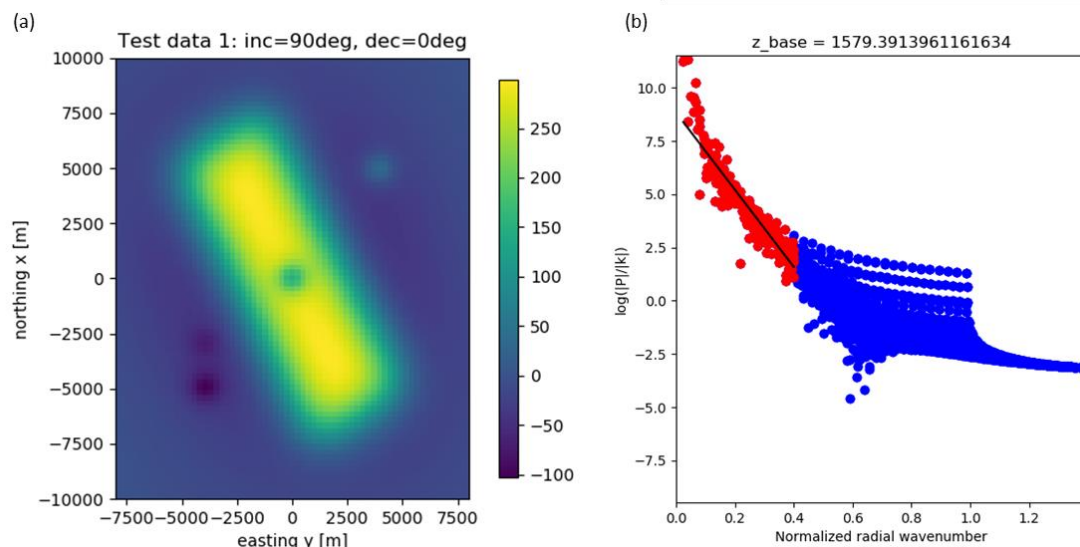


Figure 8: (a) Synthetic magnetic data from model with a deep, ridge-like feature, and 4 shallow features. (b) Radial wavenumber spectrum of the data in (a). The red dots indicate the wavenumber range used to estimate the base of the magnetic sources.

Inversion of magnetic data for magnetization and
source depth

Doc. No.

Valid from:
2021-12-07

Rev. no.

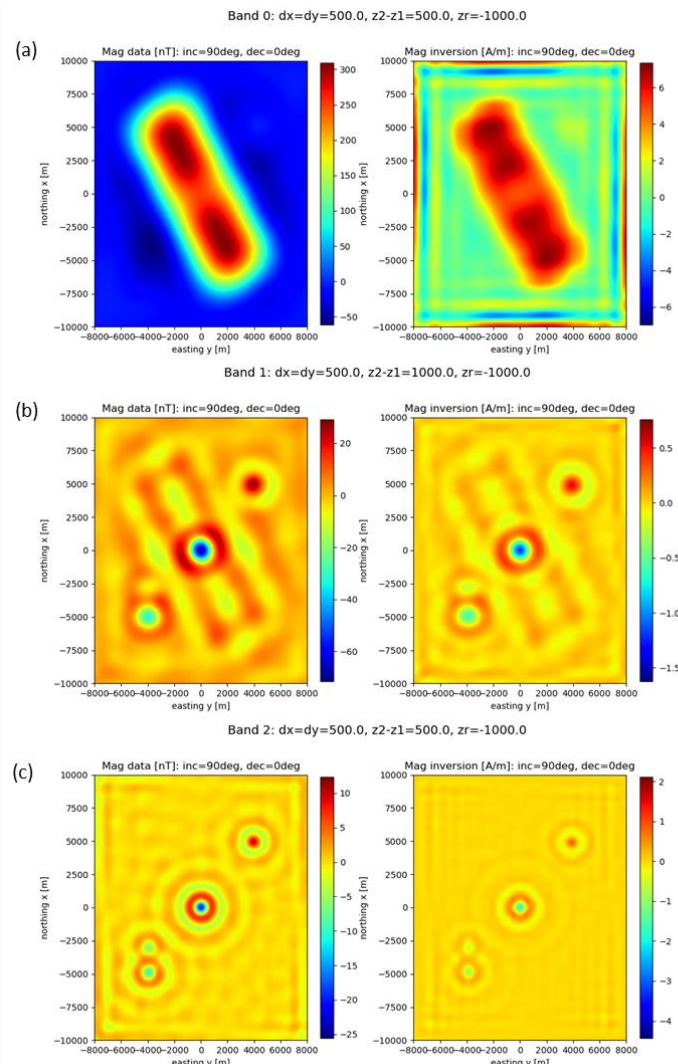


Figure 9: Inversion of three wavenumber bands. Input magnetic data in left column, and output magnetization in right column. (a) Low wavenumbers (0-15% of Nyquist), (b) intermediate wavenumbers (15-30% of Nyquist), and (c) high wavenumbers (30-60% of Nyquist),

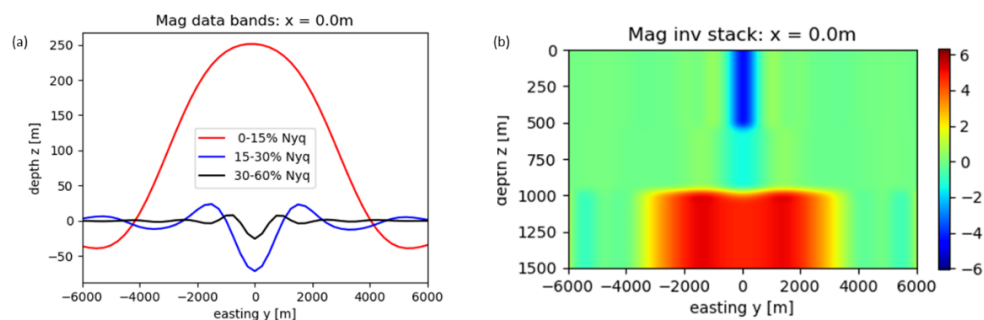


Figure 10: Vertical slice through the origin, $x = 0.0\text{m}$. (a) Magnetic anomaly data for three wavenumber ranges. (b) Stack model from after addition of the partial models from inversion of each wavenumber range separately.

6 Geothermal example

The geothermal example is from the Hellisheidi geothermal area, east of Reykjavik, Iceland. We acquired a number of magnetic lines, on foot, and by a magnetometer mounted on the car (Figure 11). Some selected lines were repeated both on foot and with car for calibration. A 45km long line, extending from Reykjanes to Selfoss (Figure 12) was used for the first test of the multi-band magnetic inversion on field data. The data was measured early in the morning, before heavy traffic started on Highway-1. Prior to the inversion, the data were corrected for the presence of the car, and edited to remove the effects of meeting cars, traffic signs, and iron poles along the road (Figure 13).

The data were decomposed into five wavenumber bands, with low, intermediate and high wavenumber ranges (Figure 14). The low wavenumbers (red line) are sensitive to the regional trend. The intermediate wavenumber ranges (black and blue lines) can be interpreted as the response of the geothermal system, and the high wavenumber (cyan and green lines) capture near-surface features. Inversion was run on the five wavenumber bands separately, and stacked to obtain an estimate of the depth-dependent subsurface magnetization (Figure 15). The magnetization profile shows the Hengill volcano in the central part of the image, with an imprint of shallow magnetic anomalies. The Hellisheidi power plant is located at approximately 22 km on the image. Towards the west (left) and east (right) ends of the profile, the magnetization tapers off in the lowlands near Reykjavik and Selfoss, respectively.



Figure 11: Magnetic data acquisition, on foot, and with magnetometer mounted on a car (Photo: Björn M. Sæther, Equinor).

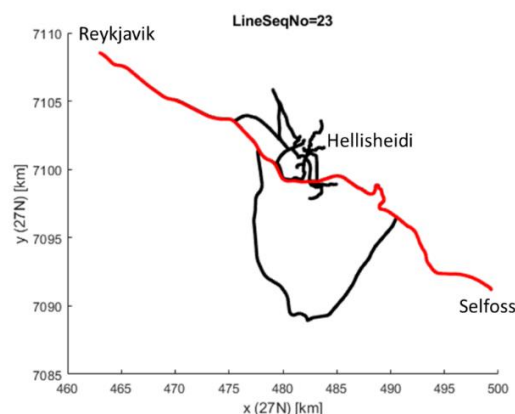


Figure 12: Magnetic lines measured in the Hellisheidi area, with the long-line from Reykjavik to Selfoss highlighted.

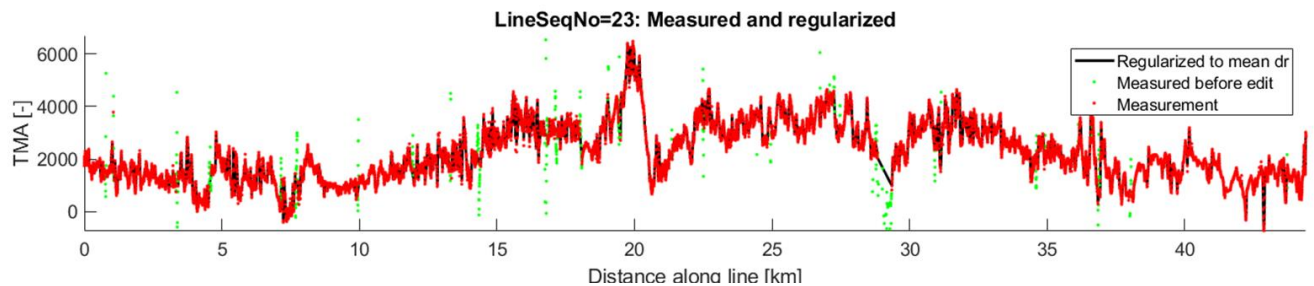


Figure 13: Magnetic data measured with a car along Highway-1 between Reykjavik and Selfoss. Data after correction for the presence of the car and subtraction of the background field (green), after editing magnetic noise from meeting cars, traffic signs and iron poles (red), and regularized to constant sample spacing of 25m (black).

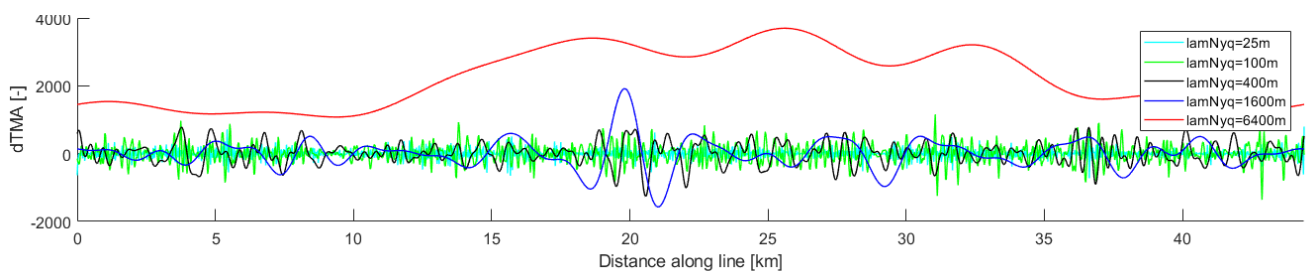


Figure 14: The regularized data in Figure 13 decomposed into five wavenumber bands.

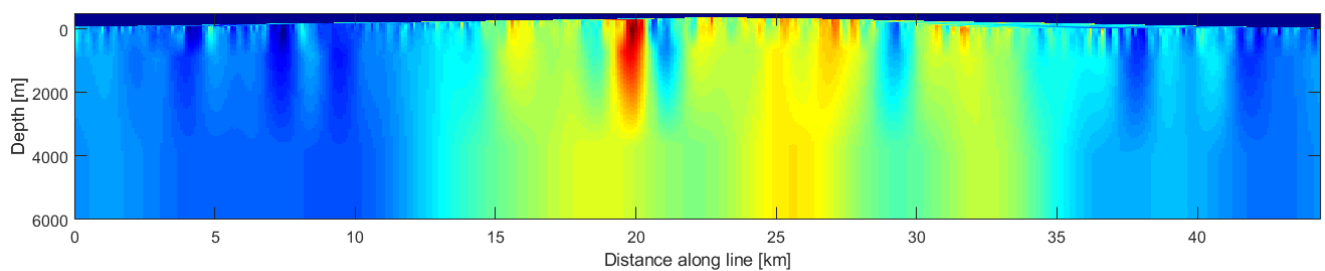


Figure 15: Magnetic model after inversion of each wavenumber band in Figure 14, and stack of the partial inversion results.

7 Seabed massive sulfide example

Seabed massive sulfides and geothermal systems are both related to hydrothermal circulation and reactive transport. However, from a magnetic point of view, there is a major difference. In general, the interpretation of magnetic (and gravity) data is challenging due to the ambiguity of big-and-shallow versus small-and-deep anomaly. Both cases may lead to the same (or at least similar) responses in the data. For seabed massive sulfides, however, the situation is different, since the water layer, the ocean, contain no magnetic anomalies. Hence, different from the onshore geothermal case, the big-and-shallow case can be excluded (Figure 16). This can be utilized in the magnetic inversion.

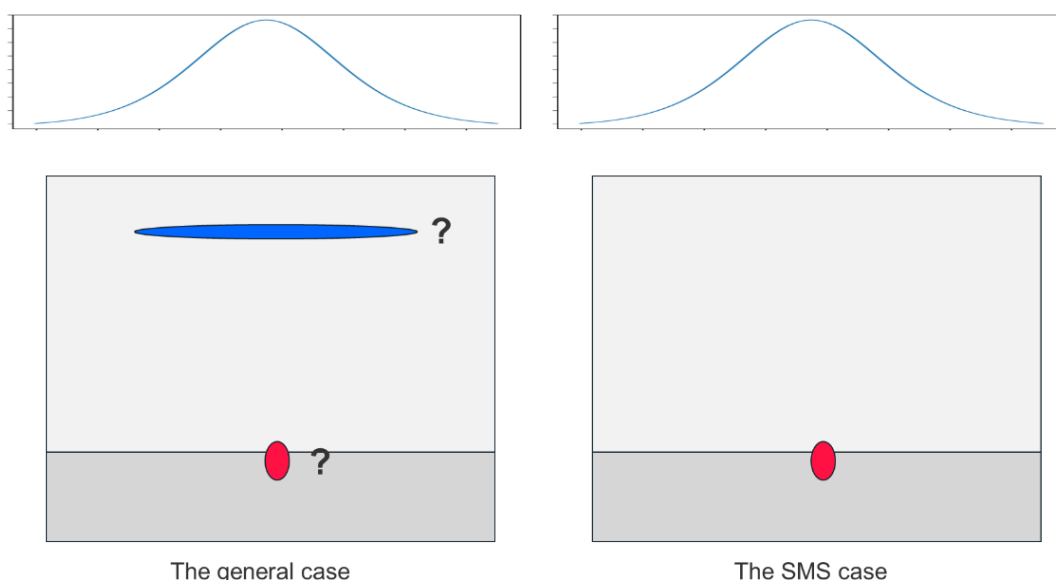


Figure 16: The big-and-shallow versus small-and-deep ambiguity in magnetic data. For seabed massive sulfides, we can exclude the big-and-shallow case and use this as a constraint in the inversion.

The most accurate magnetic mapping of seabed massive sulfides is obtained using an autonomous underwater vehicle (AUV) close to the seabed. In 2016, the MarMine project at NTNU acquired AUV magnetic data at the Mohn's Ridge (Lim et al., 2019). Equinor has access to the data, as sponsors of the project. We ran inversion of total magnetic anomaly (TMA) data from one of the AUV dives south of Loki's Castle, using the inversion described above (Figure 17). We estimated the thickness of the magnetic source layer to approximately 500m, using equations (29)-(31), and with the measured bathymetry as the upper boundary. The local present-day inclination and declination was used in the inversion, to adjust anomalies to the correct location.

Seabed massive sulfides are associated with local magnetic lows, since metal sulfides are non-magnetic. However, post-depositional processes alter the magnetic properties of basaltic rocks (Pariso and Johnsen, 1991), and minerals from hydrothermal alteration also tend to be demagnetized (Figure 18). Hence, the presence of sulfide mounds cannot be proven using magnetic data alone. A multigeophysical approach (Hokstad, 2017), where magnetic data is one of the components, may be used to increase the confidence in the interpretation, in order to detect seabed massive sulfide deposits.

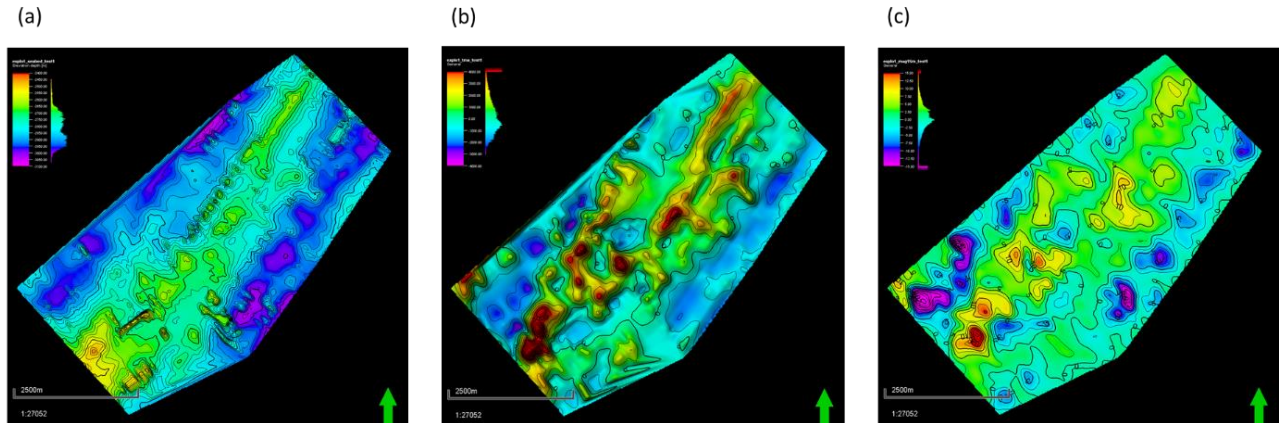


Figure 17: AUV magnetic data acquired by NTNU MarMine project at approximately 2500-3500m waterdepth on the Mohn's Ridge. (a) Bathymetry. (b) Total magnetic anomaly (TMA). (c) Magnetization from inversion.

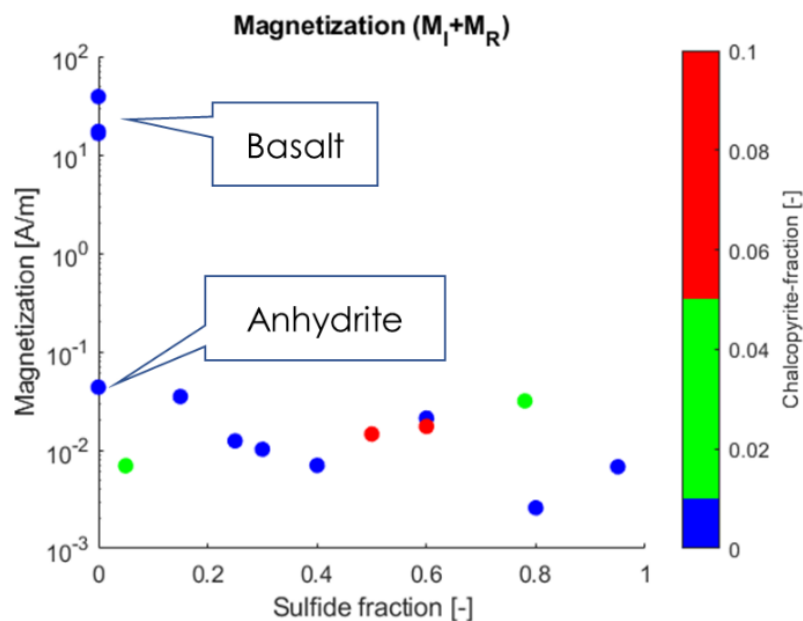


Figure 18: Magnetization measured on samples from ODP Leg 158 on the Transatlantic Geotraverse (TAG). The horizontal axis shows total sulfide fraction (including pyrite), and the samples are colored according to the chalcopyrite fraction.

When shallow magnetic anomalies are analyzed and interpreted, it's useful, and sometimes necessary know the large-scale background magnetization in which the shallow anomaly sits. Regional magnetic surveys are usually acquired by airborne magnetometers, and for the Mid-Atlantic Ridge, with water depth of order 2-3000m (Figure 19), it means that the measurements are taken at large distance from the sources. Hence, it may be expected that aeromagnetic data can reveal the regional trend, but cannot give much information about small and shallow anomalies. On the other hand, the synthetic examples above demonstrated that magnetic inversion has a focusing effect (analog to seismic imaging). To investigate this, we inverted a portion of aeromagnetic data measured over the Mohn's Ridge, and containing the area covered by the AUV magnetic data discussed previously. The data was interpolated to a horizontal sampling of 500m in

Inversion of magnetic data for magnetization and source depth

Doc. No.

Valid from:
2021-12-07

Rev. no.

x- and y-directions. The Bruhnes-Matuyama and Matuyama-Gauss magnetic reversals can be identified in the magnetic data, assuming a spreading rate of 15 mm/a (Figure 19).

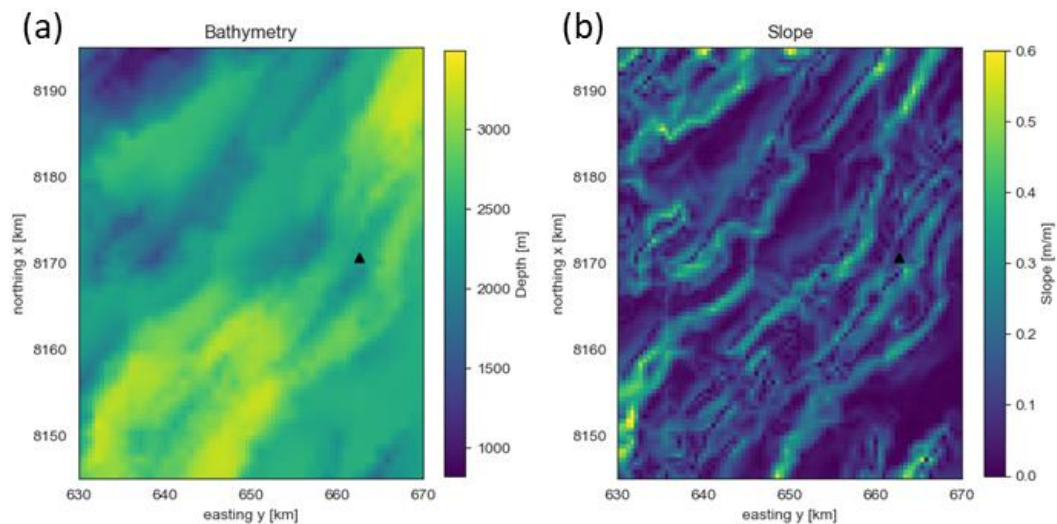


Figure 19. (a) Bathymetry and (b) slope for the area of interest on the Mohn's Ridge. The black triangle shows the location of the Loki's Castle black smoker.

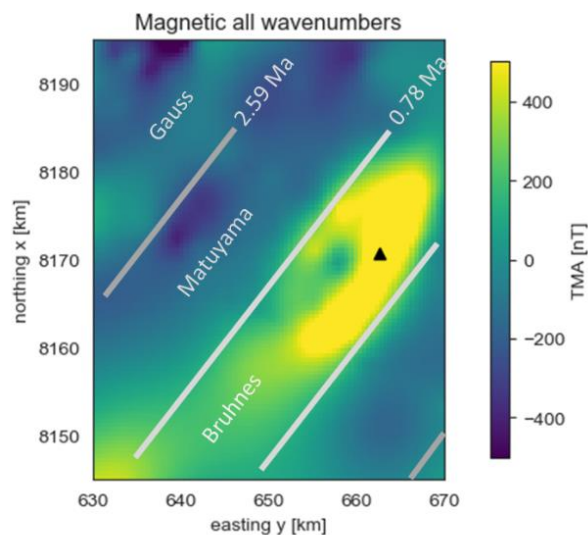


Figure 20. Aeromagnetic data from the Mohn's Ridge. The Gray lines indicate approximately the Bruhnes-Matuyama and Matuyama-Gauss magnetic reversals, calculated with a constant spreading rate of 15 mm/a. The black triangle shows the location of the Loki's Castle black smoker

We applied the same methodology as demonstrated on the Hellisheidi geothermal area on Iceland (Figure 8 to Figure 10). The aeromagnetic data was decomposed into three bands of low, intermediate and high wavenumbers, equivalent to long, intermediate and short wavelengths. The wavenumber ranges were 0-10%, 10%-20% and 20%-50% of the Nyquist wavenumber $\pi/\Delta x$, respectively. The various wavenumber bands were inverted independently (Figure 21), with varying horizontal resolutions as suitable for the different wavenumber ranges (horizontal sampling of 3000m, 2000m, and

1000m, respectively). The seabed was taken as the top of the magnetic source layer. The base of the magnetic source layer was guided by power spectral analysis, and varying with wavenumber range (8000m, 2000m and 500m below the seabed, respectively). The Marquardt-Levenberg regularization parameter λ was increased with increasing wavenumber (λ equal to 10^{-4} , 10^{-3} and 10^{-2} , respectively). For the higher wavenumber range, the tuning of the regularization parameter is a trade-off between increased resolution and stability of the inversion (Figure 22).

The results from the inversion of the data in different wavenumber ranges can be stacked to get an impression of the depth-dependence of the magnetization, though with an uncertain depth scale. An east-west oriented vertical section through Loki's Castle shows that no clear magnetic anomaly is associated with the black smoker system at the resolution obtained from the aeromagnetic data (Figure 23). However, a small low-magnetic anomaly can be observed in the high-wavenumber data.

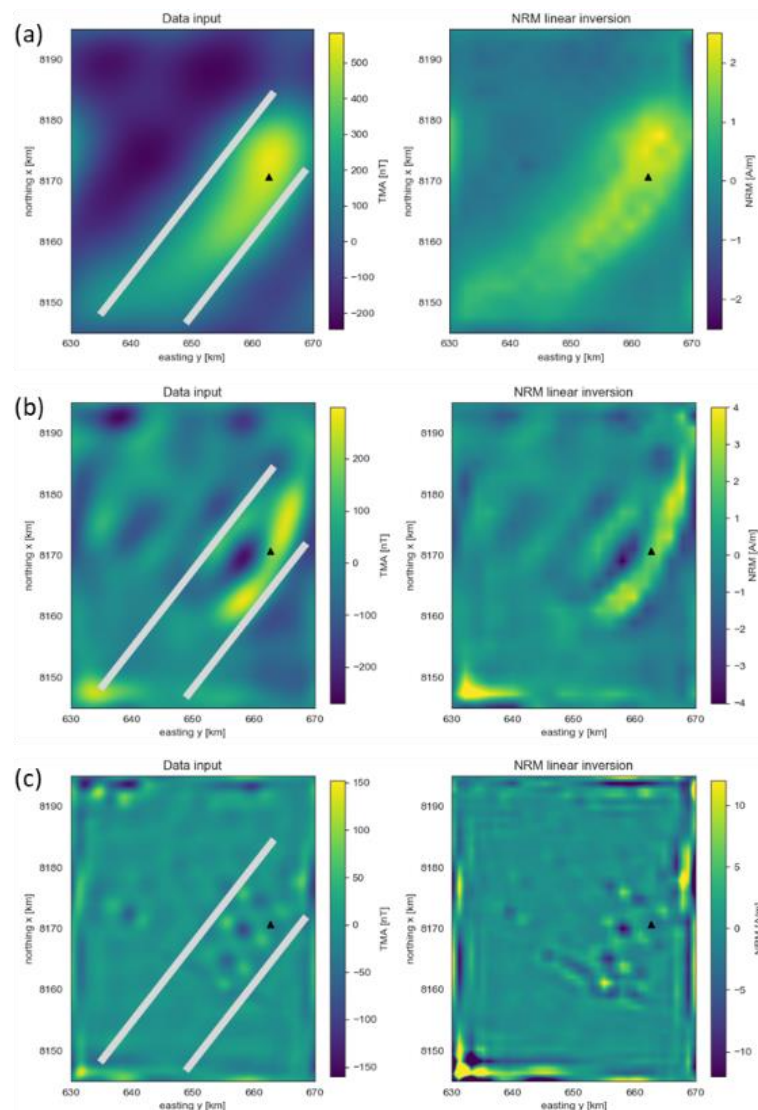


Figure 21. Aeromagnetic data decomposed in three wavenumber ranges (left column) and output from inversion (right column). (a) Low wavenumbers, (b) intermediate wavenumbers and (c) high wavenumbers. The gray liens indicate approximately the Bruhnes-Matuyama magnetic reversal. The black triangle is the location of Loki's Castle.

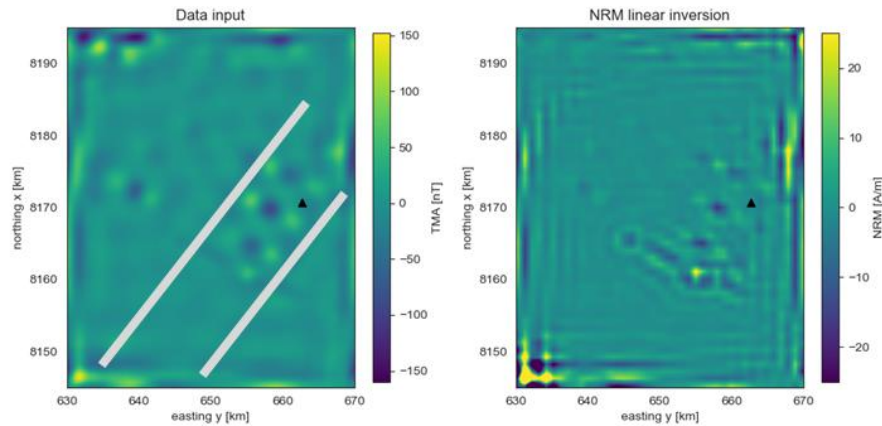


Figure 22. Reducing the regularization parameter λ , gives higher resolution, but also introduce illposedness and stability challenges (lower rank) in the inversion. High wavenumber range of the magnetic data (left) and magnetization from inversion (right).

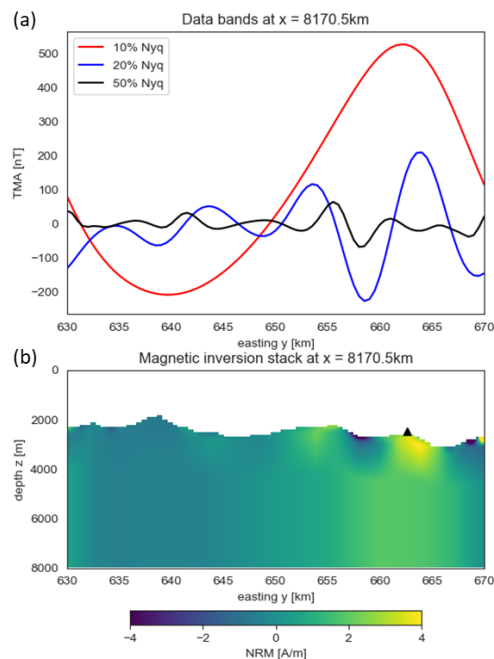


Figure 23. Aeromagnetic data from Mohn's Ridge. Stack of magnetization from inversion of low, intermediate and high wavenumber bands. East-west vertical section running through the location of the Loki's Castle black smoker.

In a modeling study performed in co-operation with NGU, a Mohn's Ridge-like geological model was built, and gravity and magnetic data were simulated, with various acquisition geometries. The seabed was represented by the real bathymetry from Mohn's Ridge. A number of simulated SMS bodies, with as size of (500m)³ were built into the model, including bodies at the known locations of Loki's Castle and Mohn's Treasure. The modeling study indicated that SMS targets can not be resolved from shipborne or airborne magnetic data measured above the sea surface. The data was decomposed into three wavenumber bands and inverted in the same way as the real data above. The result confirms that a small SMS target, such as Loki's Castle can not be resolved by inversion of magnetic data measured from surface vessels or airplanes.

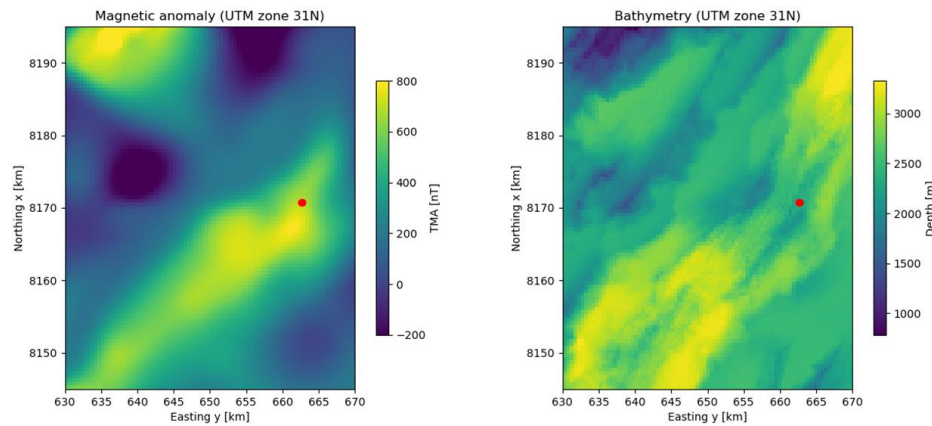


Figure 24. Simulated aeromagnetic data and bathymetry from the NGU model. The red dot indicates the location of Loki's Castle.

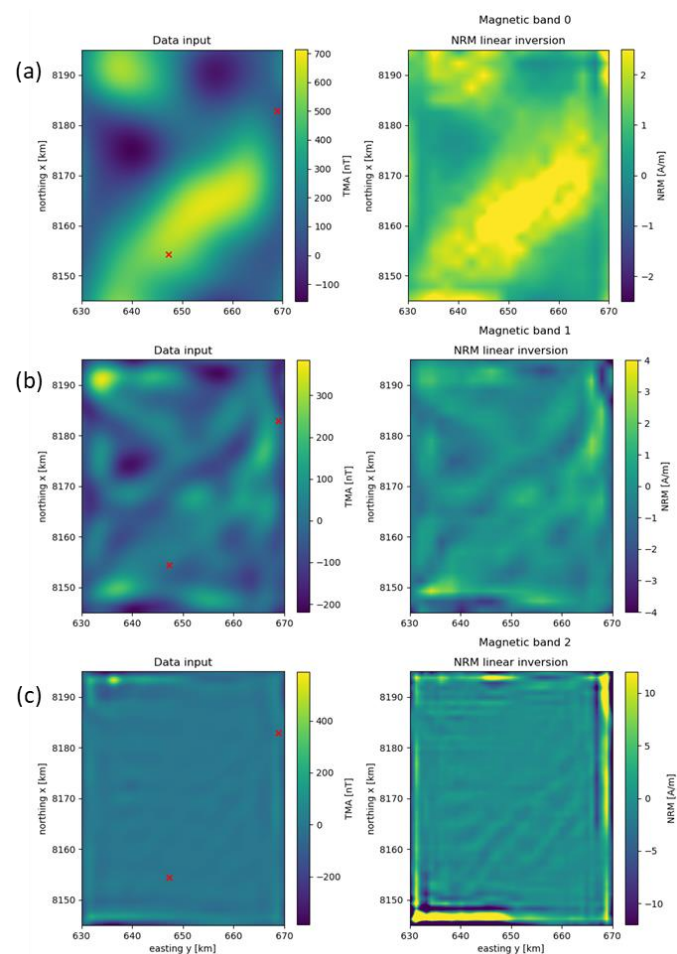


Figure 25. Synthetic aeromagnetic data from the NGU model decomposed in three wavenumber ranges (left column) and output from inversion (right column). (a) Low wavenumbers, (b) intermediate wavenumbers and (c) high wavenumbers.

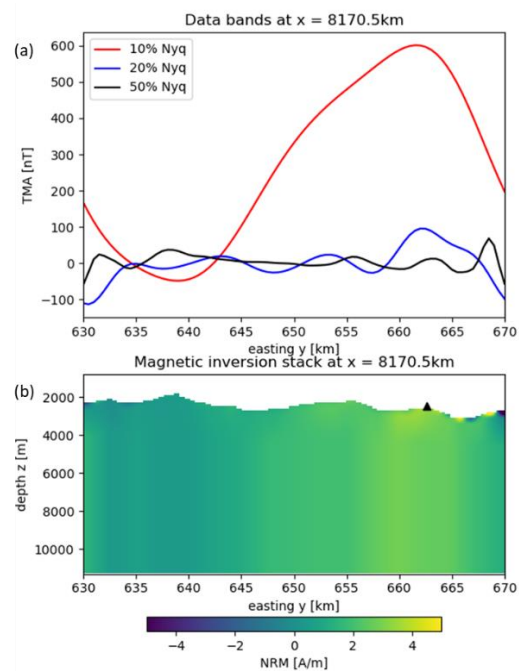


Figure 26. Synthetic aeromagnetic data from the Mohn's Ridge-like NGU model. Stack of magnetization from inversion of low, intermediate and high wavenumber bands. East-west vertical section running through the location of the Loki's Castle black smoker.

8 Conclusions

Methodology for numerical inversion of magnetic potential field data has been presented. The inverse problem is represented in the form of a map inversion, where the unknown quantity of interest is average the magnetization within a magnetic source layer. This formulation naturally also allows for estimation of the depth to the base of the magnetic source layer.

Inversion for magnetization, with a fixed source depth is a linear inverse problem, which can be solved in one step. Inversion for the base of the magnetic source layer is a non-linear inverse problem, which can be solved iteratively by Gauss-Newton iterations. Two different inversion strategies can be used: (1) Linear inversion for magnetization with fixed base of source layer, followed by iterative updates of the base with fixed magnetization. (2) Simultaneous iterative updates of both magnetization and depth of source layer. The first alternative is more robust. In both cases, the first iteration is a linear inversion step, provided the initial value for the magnetic anomaly is zero. Matrix inversions are performed using the Moore-Penrose pseudo inverse, and the Marquardt-Levenberg algorithm, which is stable and robust. Computer codes were implemented in Python, using linear algebra and Fourier transform in the numpy and scipy modules.

It is well-known that inversion of potential field data (gravity and magnetics) constitutes an illposed inverse problem. The information available in potential field data is quite limited, since different from e.g. seismic data, there is no temporal bandwidth. However, Potential field data provides a range of spatial wavenumbers (or wavelengths). The magnetic flux decays like inverse distance cube away from magnetic sources. Therefore, the size of magnetic targets that can be resolved depends on the distance from the magnetic source to the measurement surface. Small wavenumbers (large wavelengths) are sensitive to deep structure, whereas high wavenumbers (short wavelengths) are sensitive only to shallow features. To utilize these properties, an inversion strategy based on decomposition of magnetic data in radial wavenumber bands was developed. In this way, some information about the depth of the magnetic sources can be obtained

The magnetic inversion scheme is demonstrated on a number of synthetic and real data examples, with expected results. The magnetization obtained from inversion of magnetic data will subsequently be input to a second inversion step, to estimate temperature and hydrothermal alteration of basaltic rocks. This will be presented in a separate report. The proposed magnetic inversion scheme can easily be adapted for gravity inversion, by replacing the magnetic forward modeling function by the corresponding gravity forward model.

9 Acknowledgements

Part of this research was supported by the EU H2020 projects DEEPEGs Grant Agreement No 690771, and DEEPEN Grant Agreement No xxxxxx.

10 References

- Berkhout, A.J., and Verschuur, D.J., 2001, Seismic imaging beyond depth migration, *Geophysics*, **66**, 1895-1912.
- Bhattacharyya, B., 1964, Magnetic anomalies due to prism-shaped bodies with arbitrary polarizations: *Geophysics*, **4**, 29.
- Blakely, R., 1996, Potential theory in gravity and magnetic applications: Cambridge University Press.
- Dietze, F., A. Kotny, I. Heyde, and C. Vahle, 2010, Magnetic anomalies and rock magnetism of basalts from Reykjanes (SW-Iceland): *Studia Geophysica et Geodaetica*, **55**, 109-130.
- Etgen, J., Gray, S., and Zhang, Y., 2009, An overview of depth imaging in exploration geophysics, *Geophysics*, **74**, WCA5-WCA17.
- Friðleifsson G.Ó., and A. Albertsson, 2000, Deep geothermal drilling on the Reykjanes Ridge: opportunity for international collaboration: Presented at the World Geothermal Congress, Proceedings.
- Friðleifsson, G.Ó., et al., 2018, The Iceland Deep Drilling Project at Reykjanes: Drilling into the root zone of a black smoker analog, *J. Volcanol. Geotherm. Res*
- Fujimoto, K., and Kikawa, E., 1989, Alteration of Titanomagnetites and Its Related Magnetic Properties in the Noya Geothermal Area, Central Kyushu, Japan, *J.Geomag. Geoelectr.* **41**, 39-64
- Hokstad, K., Tašárová, Z.A., Clark, S.A., Kyrkjebø, R., Duffaut, K., Fichler, C. & Wiik, T. 2017: Radiogenic heat production in the crust from inversion of gravity and magnetic data. *Norwegian Journal of Geology* **97**, 241–254.
- Hokstad, K., 2017, Method of estimating a mineral content of a geological structure. Pat. App. P6716GB 142560.
- Hokstad, K., and K. Tānavsuu-Milkeviciene, 2017, Temperature prediction by multigeophysical inversion: Application to the IDDP-2 well at Reykjanes, Iceland: *GRC Transactions*, **42**, 1141- 1152.
- Hokstad, K., Alasonati Tašárová, Z., Sæther, B.M. and Tānavsuu-Milkeviciene, K., 2020, Inversion of Magnetic Data for Subsurface Temperature. *World Geothermal Congress, Reykjavik 2020* (postponed to 2021 due to COVID-19).
- Hsieh, H.-H., Chen, C.-H., Lin, P.-L., and Yen, H.-Y., 2014, Curie point depth from spectral analysis of magnetic data in Taiwan: *J.Asian Earth Science*, **90**, 26-33.
- Ising, E., 1925, Beitrag zur theorie des ferromagnetismus: *Z.Phys*, **31**, 253-258.
- Johnson, H.P., and Hall, J.M., 1977, A detailed rock magnetic and opaque mineralogy study of the basalts from the Nazca Plate, *Geophys. J. R. astr. Soc.*, **52**, 45-64.
- Kristjansson, L., and G. Jonsson, 2007, Paleomagnetism and magnetic anomalies in Iceland: *J. Geodynamics*, **43**, 30-54.
- Lattard, D., R. Engelmann, A. Kontny, and U. Sauerzapf, 2006, Curie temperatures of synthetic titanomagnetites in the Fe-Ti-O system: Effects of composition, crystal chemistry, and thermomagnetic methods: *J. Geophys. Res.*, **111**.
- Li, Y., and D. Oldenburg, 1996, 3-D inversion of magnetic data: *Geophysics*, **61**, 394-408.
- Lilleborge, M., R. Hauge, and J. Eidsvik, 2015, Information gathering in Bayesian networks applied to petroleum prospecting: *Mathematical Geosciences*, **48**, 233-257.
- Ludvigsen, M., Aasly, K., Ellefmo, S., Hilario, A., Ramirez-Llodra, E., Søreide, F., Falcon-Suarez, I., Juliani, C., Kieswetter, A., Lim, A., Malmquist, C., Nornes, S.M., Paulsen, E., Reimers, H., Sture, Ø., 2016, MarMine Cruise Report: Arctic Mid-Ocean Ridge (AMOR), NTNU Cruise reports 2016 no 1.
- Lim, A., Brønner, M., Johnsen, S.E., Dumais, M.-A., 2019, Hydrothermal activity at the ultraslow-spreading Mohns Ridge: New insights from near-seafloor magnetics, *Geochemistry, Geophysics, Geosystems*, **20**.

Inversion of magnetic data for magnetization and
source depth

Doc. No.

Valid from:
2021-12-07

Rev. no.

-
- McElhinny, M.W., and McFadden, P.L.(eds), 2000, Paleomagnetism: Continents and Oceans, International Geophysics Vol 73, Chap. 2, Elsevier Inc.
- Miracle, D., and O. Senkov, 2017, A critical review of high entropy alloys and related concepts: Acta Materialia, **122**, 448-511.
- Nagata, T., S. Uyeda, and S. Akimoto, 1952, Self-reversal of thermo-remanent magnetism of igneous rocks: J. Geomag and Geoelectricity, **4**, 22-38.
- Olivia-Urcia, B., Kontny, A., Vahle, C., and Schleicher, A.M, 2011, Modification of the magnetic mineralogy in basalts due to fluid-rock interactions in a high-temperature geothermal system (Krafla, Iceland), Geophys. J. Int., **186**, 155-174.
- Pariso, J.E., and Johnson, H.P., 1991, Alteration processes at Deep Sea Drilling Project/Ocean Drilling Program Hole 504B at the Costa Rica Rift: Implications for magnetization of oceanic crust, J. Geophys. Res., **96**, 11703-11722.
- Quesnel, Y., Lanflais, B., Sotin, C., and Galdeano, A., 2008, Modelling and inversion of local magnetic anomalies, J. Geophys & Eng., **5**, 387-400
- Stacey, F., 1974, The physical principles of rock magnetism: Elsevier.
- Szitkar, F., Dymant, J., Fouquet, Y. and Choi, Y., 2014, What causes low magnetization at basalt-hosted hydrothermal sites? Insights from inactive site Krasnov (MAR 16°38'N), Geochem. Geophys. Geosyst. **15**, 1441–1451.
- Tänavsuu-Milkeviciene, K., K. Hokstad, I. Merciu, and C. Kruber, 2018, Understanding geothermal reservoirs: IDDP-2, Iceland: Presented at the AAPG GTW Series, Proceedings.
- Vine, F., and D. Matthews, 1963, Magnetic anomalies over oceanic ridges: Nature, **199**, 947-949.
- Wise, A., M. Saenko, A. Valazquez, D. Laughlin, M. Daiz-Michelena, and M. McHenry, 2011, Phase evolution in the Fe₃O₄-Fe₂TiO₄ pseudo-binary system and its implications for remanent magnetization in martian minerals: IEEE Transactions on Magnetism, **47**, 4124-4127.
- Yund, R., and R. McAllister, 1969, Kinetics and mechanisms of exsolution: Chemical Geology, **6**, 5-30.

11 Appendix: Gravity forward model

In the appendix, we outline how the magnetic inversion scheme presented above can easily be adapted to conventional gravity data, as well as vertical gravity gradients. Gravity anomaly data are due to monopole density sources in the subsurface. The anomalous vertical gravity field \mathbf{g}_z can be obtained by differentiation of an inverse-distance potential (Blakely, 1996)

$$\mathbf{G}(\mathbf{x}) = -\gamma \nabla \iiint \frac{\rho(\mathbf{x}')}{|\mathbf{x}' - \mathbf{x}|} dV', \quad (35)$$

where ρ is the density, and γ is the gravity constant. As for the magnetization discussed above, we assume that the density is independent of depth, or it represents an average over the depth range of interest z_1 to z_2 , such that

$$\rho(x, y) = \frac{1}{z_2 - z_1} \int_{z_1}^{z_2} \rho(x, y, z) dz. \quad (36)$$

Integrating source depth z' over the interval of interest z_1 to z_2 , and using equations above, the vertical component of the gravity field can be approximated as

$$G_z(\mathbf{x}) \simeq \gamma \iint a_z(\mathbf{x}, \mathbf{x}') \rho(\mathbf{x}', y') dx' dy', \quad (37)$$

where

$$a_z = \frac{\partial F(z_2)}{\partial z} - \frac{\partial F(z_1)}{\partial z}, \quad (38)$$

and

$$\frac{\partial F(z')}{\partial z} = -\frac{\partial F(z')}{\partial z'} = -\frac{1}{r}. \quad (39)$$

The vertical derivative of the gravity field can be written as

$$G_{zz}(\mathbf{x}) = \frac{\partial G_z}{\partial z} \simeq \gamma \iint A_{zz}(\mathbf{x}, \mathbf{x}') \rho(\mathbf{x}', y') dx' dy', \quad (40)$$

For later use in inversion, we discretize the integral over density sources. Then the forward model for the gravity anomaly observed at location \mathbf{x}_i due to density sources at \mathbf{x}'_j can be written as

$$G_z(\mathbf{x}_i) = \sum_j Q_z(\mathbf{x}_i, \mathbf{x}'_j) \rho(\mathbf{x}'_j), \quad (41)$$

where

$$Q_z(\mathbf{x}_i, \mathbf{x}'_j) = \gamma \Delta S'_j a_z(\mathbf{x}_i, \mathbf{x}'_j). \quad (42)$$

The forward model for the vertical derivative of the gravity field can correspondingly be written as

$$G_{zz}(\mathbf{x}_i) = \sum_j Q_{zz}(\mathbf{x}_i, \mathbf{x}'_j) \rho(\mathbf{x}'_j), \quad (43)$$

where

$$Q_{zz}(\mathbf{x}_i, \mathbf{x}'_j) = \gamma \Delta S'_j A_{zz}(\mathbf{x}_i, \mathbf{x}'_j). \quad (44)$$

Inversion of magnetic data for magnetization and
source depth

Doc. No.

Valid from:
2021-12-07

Rev. no.
